

## Research Article

# High Precise Scattering Centers Models for Cone-Shaped Targets Based on Induced Currents

Qi-Feng Li,<sup>1</sup> Kun-Yi Guo,<sup>1</sup> Xin-Qing Sheng,<sup>1</sup> and Tian-Shu Liu<sup>2</sup>

<sup>1</sup>Center for Electromagnetic Simulation, School of Information and Electronics, Beijing Institute of Technology, Beijing, China

<sup>2</sup>Science and Technology on Special System Simulation Laboratory, Beijing Simulation Center, Beijing 100854, China

Correspondence should be addressed to Kun-Yi Guo; guokunyi@bit.edu.cn

Received 6 November 2016; Accepted 28 December 2016; Published 7 March 2017

Academic Editor: Yumao Wu

Copyright © 2017 Qi-Feng Li et al. This is an open access article distributed under the Creative Commons Attribution License, which permits unrestricted use, distribution, and reproduction in any medium, provided the original work is properly cited.

Based on induced currents of cone-shaped targets, the high precise scattering center model is derived in this paper. The distribution characteristics of the induced currents and their relationships with the attributes of scattering centers are investigated in detail; the high precise scattering center model is obtained. In order to validate the scattering center model, numerical simulations of two cone-shaped targets are presented, and the accuracies of the models are validated through comparing the range profiles simulated by the models with those by a full-wave numerical method. The validation results demonstrate that this model is superior to the existing model in precisely characterizing the scattering centers induced by creeping waves.

## 1. Introduction

Scattered fields of radar targets at sufficiently high frequencies can be approximated as the sum of scattered fields from individual scattering sources, and these scattering sources are generally called scattering centers [1]. The term of scattering center has been expanded for now. Scattering phenomena under cases of lower frequency, creeping waves, for example, can also be described in terms of scattering centers and these scattering centers are also significant scattering components in some conditions [2, 3]. The characteristics of radar returns from a target are primarily determined by the attributes of its scattering centers, such as locations and scattering amplitudes, and their dependencies on aspect angle, frequency, and polarization [4]. Therefore, parametric scattering center models that concisely and precisely characterize radar returns have gained considerable attention in many radar applications, such as automatic target recognition (ATR) [5, 6] and radar image interpretation [7, 8].

Parametric scattering center model is the combination of a series of analytical functions that describe the changes of location and scattering amplitude of scattering centers with frequency and aspect angle of line of sight (LOS) of radar. The existing scattering center models for monostatic

radar configuration include the damped exponential model [9, 10], the geometrical theory of diffraction (GTD) based model [11, 12], the attributed scattering center model [13–15], and the sliding scattering center model [16]. These scattering center models are all developed for scattering problems of high frequency, such as specular reflection by large-scale smooth surface or diffraction by large-scale straight edge. The precision of these models is greatly challenged for describing the scattering problem of lower frequency, such as diffraction by small-scale edges and rescattered waves of creeping waves and travelling waves on smooth surface. And even worse, there are no generalized analytical solutions for these kinds of scattering problems.

To tackle this problem, the models of the induced currents on the target are built at first; then the scattering center model is derived by the electric field integral expression based on the current model. The modelling of the induced currents on the target is easier than the scattering center modelling, for the precise numerical results of currents can be acquired by full-wave numerical computation. The well validated full-wave numerical method, namely, the hybrid finite element-boundary integral-multilevel fast multipole algorithm (FE-BI-MLFMA) [17–20] is used in this paper. It is found that for cone-shaped target, its scattering characteristics are mainly

determined by one-dimensional (1D) currents on the lines in the plane constructed by the LOS and the rotational axis of the cone. Therefore, the modelling of the induced currents on the target is greatly simplified.

Based on the built model of the 1D currents, the relationship between the characteristics of currents and the attributes of scattering centers is investigated; the formation processes of scattering centers by its contributing currents are analyzed. It is found that one parameter of current models is sometimes related to several scattering centers, and vice versa. In other words, the coupling of multiple scattering sources has been included in the current model. Moreover, the scattering phenomena of creeping waves are also included in the current model, and the corresponding scattering center can be easily acquired based on the current model. In order to validate the presented method, numerical simulations of two cone-shaped targets are investigated in detail, and the accuracies of the built models are validated through comparing the range profiles (RPs) simulated by the models with the real RPs of the two targets computed by FE-BI-MLFMA, as well as the RPs simulated by the attributed scattering center model obtained by traditional method.

The remainder of the paper is organized as follows: Section 2 presents the modelling of the induced currents on a blunt-nosed cone target. Section 3 presents the derived scattering center model based on the current model. Section 4 presents the validation of the built scattering center models. Finally, Section 5 provides the conclusions of this paper.

## 2. Parametric Expressions of Scattering Centers

The induced currents on a cone-shaped target are investigated in this section. The cone-shaped target is a perfect electric conductor (PEC). The geometry of the cone and the relative position of the target and radar are shown in Figure 1. The body-fixed Cartesian coordinate system  $(x, y, z)$  is used to describe the geometry, its origin is at the bottom center of the target, and the rotationally symmetric axis of the cone is located along the  $z$ -axis, as shown in Figure 1. The geometrical parameters of the target are set as  $R = 0.732$  m,  $r = 0.061$  m,  $h = 3.721$  m, and  $\alpha = 10.4^\circ$ . The radar parameters are set as follows: the frequency range is  $f = 1\sim 2$  GHz, with sampling interval of  $\Delta f = 12.5$  MHz.

Suppose that the distance between the radar and the target satisfies the far-field condition ( $R_0 > 2L^2/\lambda$ , where  $R_0$  is the distance between the radar and the target and  $L$  is the size of the target). In far-field condition, the incident wave can be taken as plane wave; then the induced currents on the target illuminated by the plane waves from the monostatic radar are computed by FE-BI-MLFMA. The characteristics of currents on the flank and the bottom are investigated separately in the following.

**2.1. Characteristics of Induced Currents on the Flank.** As the cone is a rotationally symmetrical object, the change of the LOS in azimuth angle (denoted by  $\phi$ ) does not affect the characteristics of induced currents. Therefore, without loss

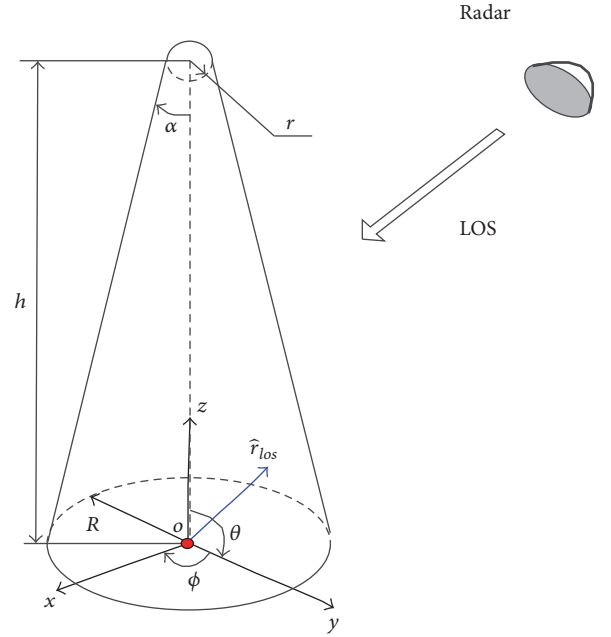


FIGURE 1: The geometry of the cone-shaped target and the radar.

of generality, we set the change of LOS to be in the  $xoz$  plane, and the elevation angle of the LOS is denoted by  $\theta$ . Then, the wave vector of incident wave can be expressed as  $\vec{k}_i = (2\pi/\lambda)(-\cos\theta\hat{z} - \sin\theta\hat{x})$ .

When the incident electric field is under vertical polarization, the magnetic field can be expressed as  $\vec{H}_i = -H_m\hat{\phi} = -H_m\hat{y}$ . The induced currents on the cone are presented in Figure 2, where the used parameters of the incident waves are  $f = 1$  GHz,  $\theta = 8^\circ$ . Figure 2(a) shows the amplitude of the induced currents and Figure 2(b)L1 is the intersection line of the flank of the cone with the plane constructed by the axis of cone and the direction of the incident electric field, and L2 is the intersection line of the flank with the plane constructed by the axis of cone and the direction of the incident magnetic field. In our geometry setting, the generatrix in  $xoz$  plane of lit region is L1 and the generatrix in  $yoz$  is L2.

As shown in Figure 2(a), the maximal values of currents are on L1 and the minimal values of currents are on L2. The conclusion agrees with the analytical results based on physical optics method (PO) [21–24]. The normals of the flank on L1 and L2 are  $\hat{n}_{L1} = \cos\alpha\hat{x} + \sin\alpha\hat{z}$  and  $\hat{n}_{L2} = \cos\alpha\hat{y} + \sin\alpha\hat{z}$ . Based on PO, induced current can be approximately expressed as  $\mathbf{J} = 2\hat{n} \times \mathbf{H}_i$ , so the currents on L1 and L2 can be derived as  $\mathbf{J}_{L1} = 2H_m(-\cos\alpha\hat{z} + \sin\alpha\hat{x})$  and  $\mathbf{J}_{L2} = 2H_m(\sin\alpha\hat{x})$ . The incident electric field is generally set as 1 V/m in computation; then the incident magnetic field is  $H_m = 1/Z$ , where  $Z$  is the wave impedance of free space.

Optical currents on L1 computed by PO method are compared with the values computed by FE-BI-MLFMA (called full-wave currents for short), as presented in Figure 3 ( $\theta = 8^\circ$ ). Figure 3(a) shows the amplitude (A/m<sup>2</sup>) of the currents, and Figure 3(b) shows the unwrapped phase (rad)

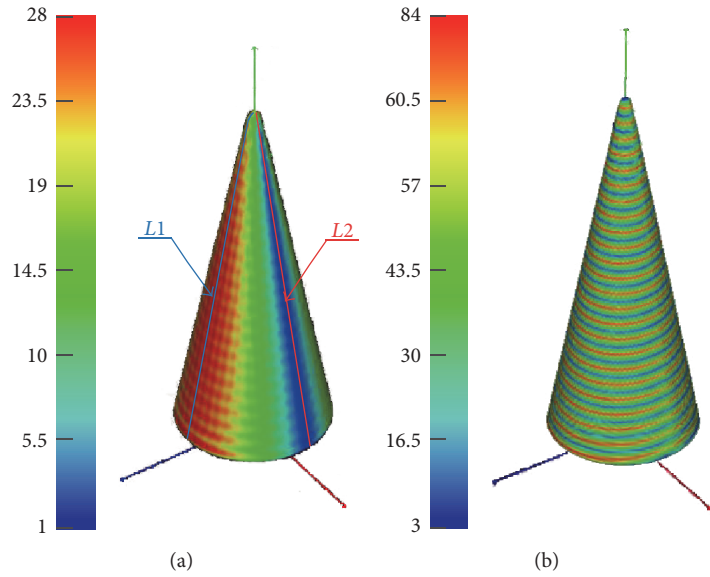


FIGURE 2: Induced currents on the flank of the cone. (a) Amplitude; (b) phase.

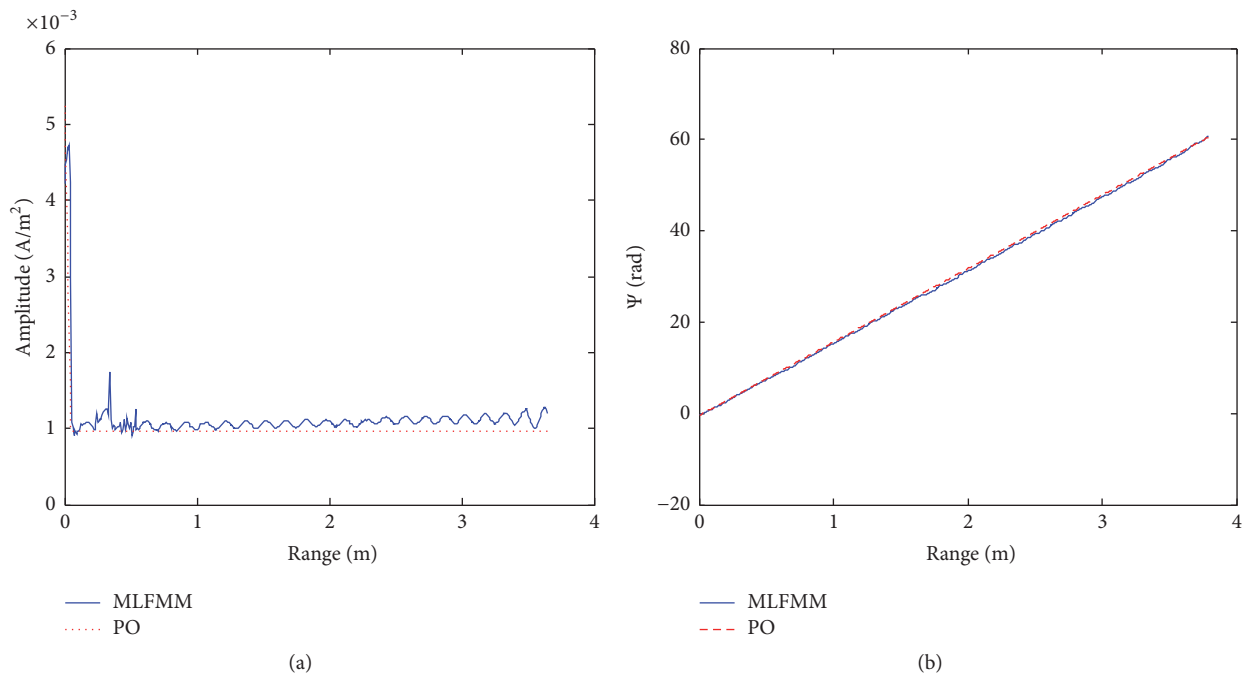


FIGURE 3: Amplitude and phase of the currents on  $L1$ . (a) Amplitude; (b) unwrapped phase.

of the currents. The range of horizontal axis indicates the distance between a point on  $L1$  and the top of the cone

Figure 3(a) shows that there are significant differences between the optical currents and the full-wave currents. The full-wave currents along  $L1$  are more complex than that of the optical currents. Near the two ends of  $L1$ , the amplitude of the full-wave currents is obviously larger than that of the optical currents. Within the internal region of  $L1$ , the amplitude fluctuates as a combination form of periodicity and linearity.

Figure 3(b) shows that the two results agree well with each other, and the phase of induced current linearly changes along  $L1$ .

The generatrix in  $xoz$  plane in shadow region is denoted by  $L1'$ . The induced currents on  $L1'$  are shown in Figure 4. The fluctuation feature and the values of the induced currents on  $L1'$  are similar to the case of  $L1$ , which means the scattering components of creeping waves are the denominated scattering contributions when the elevation angle of the LOS is

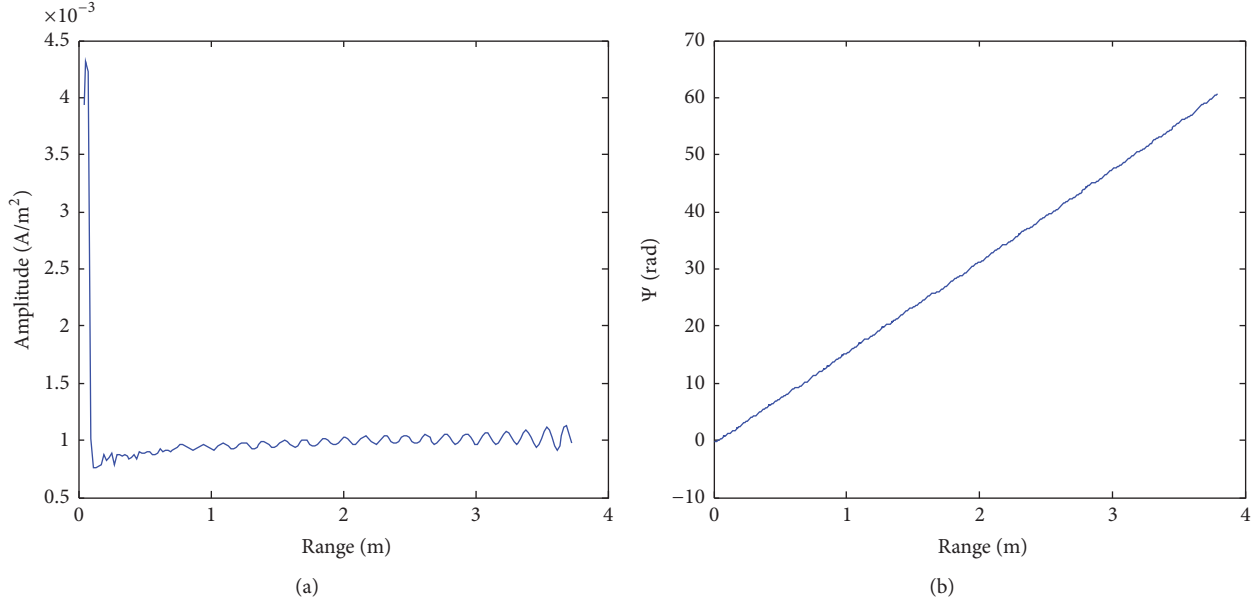


FIGURE 4: Amplitude and phase of the induced currents on  $L1'$  in shadow region. (a) Amplitude; (b) unwrapped phase.

small ( $\theta = 8^\circ < \alpha$ ). The range of horizontal axis indicates the distance between a point on  $L1'$  and the top of the cone.

Based on the characteristics of the induced currents on  $L1$  and  $L1'$  under different LOSs, the full-wave currents are described by the following expressions:

$$J(\rho, f, \theta) = A_m(\rho, f, \theta) \exp(j\phi_m(\rho, f, \theta)) \quad (1)$$

$$A_m(\rho, f, \theta) = a_{m1} \cdot \sin[a_{m2}(\theta)f\rho + a_{m3}(\theta)\rho + a_{m4}(\theta)f + a_{m5}(\theta)] + a_{m6}\rho + a_{m7} \quad (2)$$

$$\phi_m(\rho, f, \theta) = a_{m8}(\theta)f\rho + a_{m9}(\theta)\rho, \quad (3)$$

where (1) describes the complex value of induced current; its amplitude and phase are indicated by  $A_m$  and  $\phi_m$ . Equation (2) is proposed according to the amplitude characteristics of the induced currents on  $L1$  and  $L1'$  under different LOSs. Equation (3) is proposed according to the phase characteristics of the induced currents on  $L1$  and  $L1'$ .  $\rho$  indicates the position of the current element on  $L1$  ( $m = 1$ ) or  $L1'$  ( $m = 2$ ).  $A_m(\cdot)$  and  $\phi_m(\cdot)$  are the amplitude and the phase of the currents, respectively.  $a_{mn}$  ( $n = 1, 2, \dots, 9$ ) indicates the parameters to be estimated.  $a_{m1}$  is irrelevant to frequency, but  $a_{m2}$ ,  $a_{m3}$ ,  $a_{m4}$ ,  $a_{m5}$ ,  $a_{m8}$ , and  $a_{m9}$  are linear-circular correlated with  $\theta$ .

To show characteristics of the currents on the whole conical surface, we slice the cone along line  $L1$  and unfold the flank to a fan surface, as shown in Figure 5. The currents on the fan and the bottom are shown in Figure 6. The half-angle of the fan is  $\gamma = \pi R/l$ , where  $l$  is the outer radius of the fan.

Based on PO method, the two-dimensional currents can be expressed as  $\mathbf{J}(\rho, \beta) = 2\hat{n}(\beta) \times \mathbf{H}^i = 2H_m(\sin \alpha \hat{x} -$

$\cos \alpha \cos((\beta/\gamma)\pi)\hat{z})$ , where  $(\rho, \beta)$  is the coordinates of the individual current on the fan. The component of  $\mathbf{J}(\rho, \beta)$  along vertical direction ( $\hat{v} = -\cos \alpha \hat{z} + \sin \alpha \hat{x}$ ) can be expressed as (4). Therefore, the change of currents with  $\beta$  can be described by the currents on  $L1$  and the dependant function  $F(\beta)$ .

$$J_v(\rho, \beta) = J_v(\rho, 0) F(\beta) \quad (4)$$

$$F(\beta) = \left( \cos^2 \alpha \cos\left(\frac{\beta}{\gamma}\pi\right) + \sin^2 \alpha \right). \quad (5)$$

Equations (4) and (5) describe the fact that the change of induced currents with  $\beta$  can be expressed by the currents on  $L1$  and the dependent function  $F(\cdot)$ .

**2.2. Characteristics of Induced Currents on the Bottom.** Similarly, the induced currents on the bottom are investigated here. The amplitudes and phases of induced currents on the bottom are presented in Figures 7(a) and 7(b), respectively. The parameters of the incident waves are the same as those of Figure 2. The line in  $xoz$  plane along  $+x$  axis is denoted by  $I1$ , the line in  $xoz$  plane along  $-x$  axis is denoted by  $I1'$ , and the line in  $yoz$  plane along  $+y$  axis is denoted by  $I2$ . The maximal values of currents are on  $I1$  and the minimal values of currents are on  $I2$ . The scattering field from the bottom is mainly contributed by the currents on  $I1$  and  $I1'$ .

The currents on  $I1$  are presented in Figure 8. The range of horizontal axis indicates the distance between a point on  $I1$  and the point on the curved edge. From Figure 8(a), it can be seen that the amplitude of full-wave currents fluctuates as a combination form of periodicity and linearity. From Figure 8(b), it can be seen that the phase of induced current changes linearly along  $I1$ . The characteristics of the currents on  $I1'$  are similar to  $I1$ .

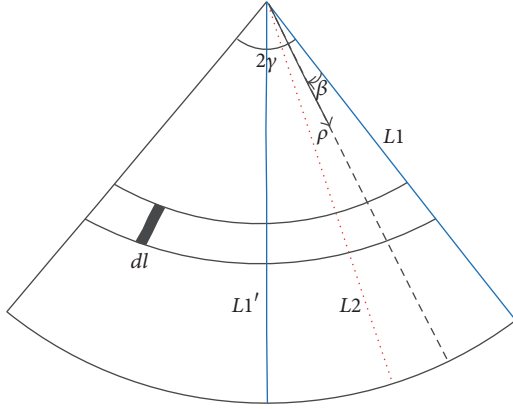


FIGURE 5: Unfolded fan.

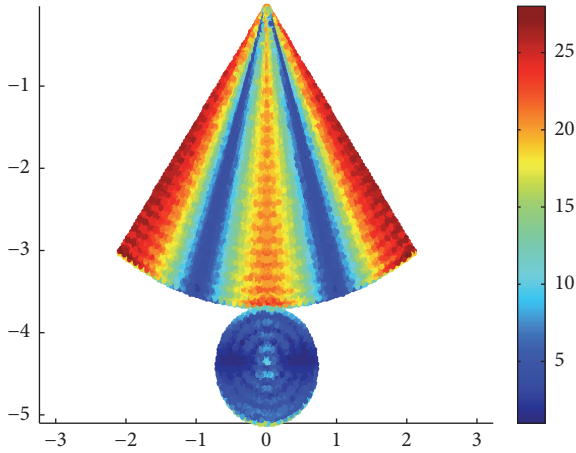


FIGURE 6: Currents on the fan and the bottom.

These characteristics of the currents on the bottom are similar to the case of currents on the flank. Therefore, the currents on the bottom are also described by the expression of (1), only with different parameters. The currents on  $I1$  and  $I1'$  are indicated by the case of  $m = 3$ . Similarly, the two-dimensional currents on the bottom are also expressed by (4).

**2.3. Estimation of the Current Model Parameters.** The coefficients in the presented formula,  $a_{m1} \sim a_{m9}$ , are estimated through matching the currents computed by the model with the currents computed by FE-BI-MLFMA. The used method for optimal estimation is genetic algorithm (GA) [25–28]. The currents on the flank computed by the model with estimated parameters (the simulated currents for short) are presented in Figures 9(a) and 10(a). For comparison, the currents computed by FE-BI-MLFMA (the real currents for short) are presented in Figures 9(b) and 10(b). The used parameters in computation are  $f = 1 \sim 2$  GHz and  $\Delta f = 0.125$  GHz,  $\theta = 8^\circ$ . The range of horizontal axis indicates the distance between a point on  $L1$  and the top of the cone.

The errors between the simulated currents and the real currents are examined: the correlation coefficient of the amplitudes is 92.81% and the root mean square error (RMSE) is  $6.01 \times 10^{-5}$  V/m<sup>2</sup>; the correlation coefficient of the unwrapped phases is 98.72% and the RMSE is 2.99 rad.

Other cases of incident angle ( $\theta = 1^\circ \sim 10^\circ$ ) are also investigated. The parameters of currents are estimated with the same method. The errors between the simulated currents and the real currents are the correlation coefficient of the amplitudes is larger than 90% and the RMSE is less than  $10^{-4}$  V/m<sup>2</sup>; the correlation coefficient of the unwrapped phases is larger than 95% and the RMSE is less than 4 rad.

### 3. Approach of Scattering Center Modelling

There are two classical methods for scattering center modelling. Scattering centers can be extracted directly from radar images by peak or pattern detection, or they can be described by parametric models and the unknown parameters of the model then be acquired through optimal estimation. The second method is not limited by radar resolutions and could provide more precise and elaborate descriptions of scattering centers, yet it is under the strict precondition of the accuracy and application scope of parametric model. The commonly used parametric models are proposed according to the solutions of several simple targets based on the physical optics method (PO) or geometrical theory of diffraction (GTD). Due to limitations of these asymptotic methods, the existing parametric models fail in some cases, for example, creep waves. In this paper, the parametric model is derived from the induced currents which are computed by a full-wave numerical method. All the scattering contributes are included in the derived model.

Based on the electric field integral expression under the far-field condition in the free space [29], the scattered field can be expressed as

$$E_v^s = -j\omega\mu N_v = -jkZN_v, \quad (6)$$

where  $Z$  is wave impedance of free space,  $N_v$  is the component of the vector  $\mathbf{N}$  along  $\hat{v}$  direction.

$$\mathbf{N} = \frac{e^{-jkr}}{4\pi r} \int \mathbf{J}(\mathbf{r}') e^{jk\mathbf{r}' \cdot \hat{r}} dS', \quad (7)$$

where  $\hat{r} = \sin\theta \cos\phi \hat{x} + \sin\theta \sin\phi \hat{y} + \cos\theta \hat{z}$  and  $\mathbf{r}' = \rho \sin\alpha \cos((\beta/\gamma)\pi) \hat{x} + \rho \sin\alpha \sin((\beta/\gamma)\pi) \hat{y} + (h - \rho \cos\alpha) \hat{z}$ .

Substituting (4) into (7), we can derive the results of the currents in lit region ( $\beta = 0 \sim \gamma$ ).

$$N_v = \frac{e^{-jkr}}{4\pi r} \int_l \int_0^\gamma J_v(\rho, 0) F(\beta) \cdot \exp \left\{ jk \left[ \cos\theta (h - \rho \cos\alpha) + \rho \sin\theta \sin\alpha \cos\left(\frac{\beta}{\gamma}\pi\right) \right] \right\} \rho d\rho d\beta. \quad (8)$$

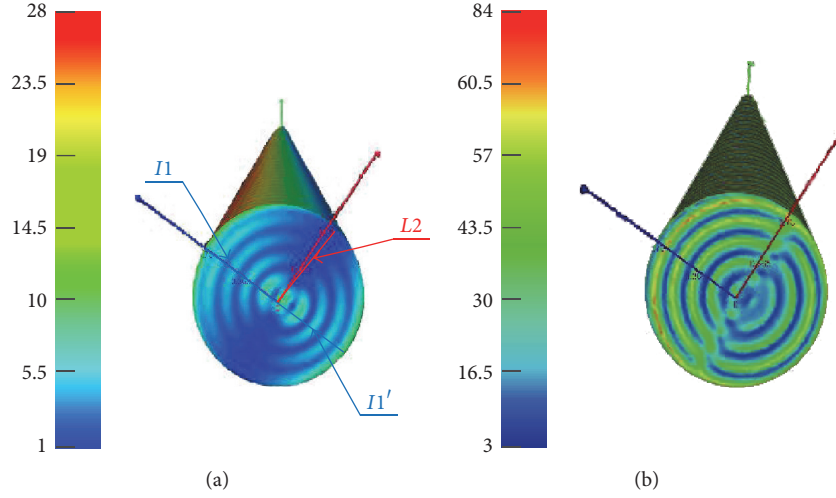


FIGURE 7: Currents on the bottom. (a) Amplitude; (b) phase.

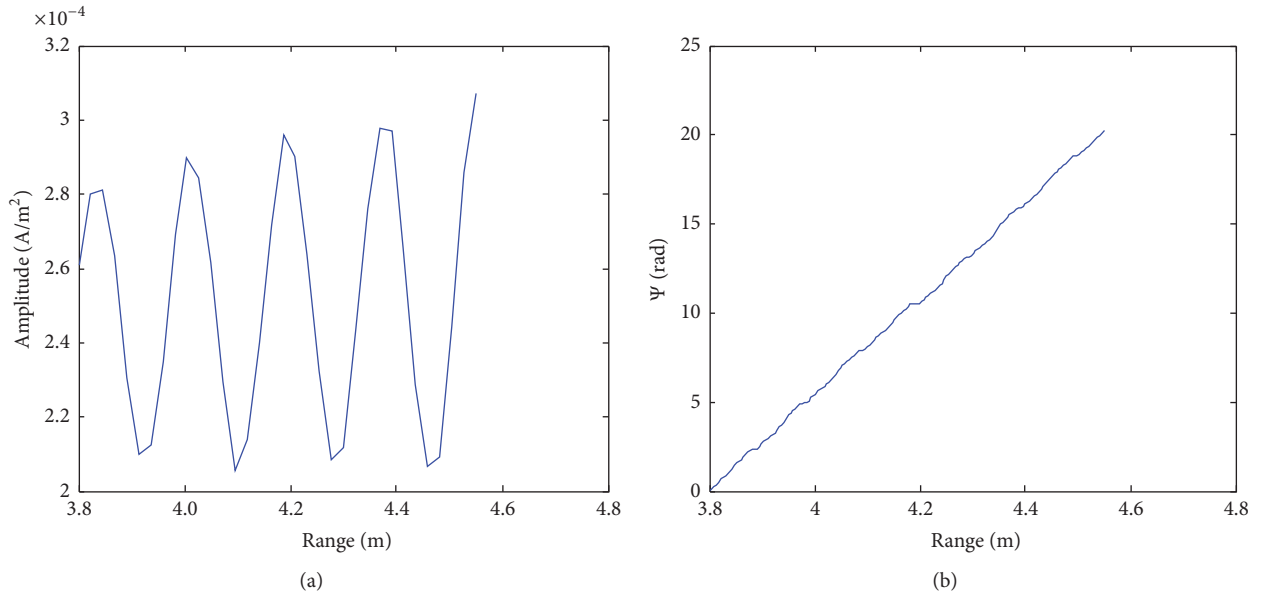


FIGURE 8: Currents on I1. (a) Amplitude; (b) unwrapped phase.

The integral part related to  $\beta$  can be derived based on the principle of stationary phase [30], as follows:

$$G(\rho) = \int_0^\gamma F(\beta) \exp \left\{ jk\rho \sin \theta \sin \alpha \cos \left( \frac{\beta}{\gamma} \pi \right) \right\} d\beta \quad (9)$$

$$\approx \sqrt{\frac{2\pi}{jk\rho \sin \theta \sin \alpha}} \exp \{ jk\rho \sin \theta \sin \alpha \}.$$

Then, the scattered field can be expressed as

$$E_v^s = -jkZ \frac{e^{-jkr}}{4\pi r} \int_I J_v(\rho, 0) \cdot \exp \{ jk \cos \theta (h - \rho \cos \alpha) \} G(\rho) \rho d\rho = -jkZ \quad (10)$$

$$\cdot \frac{e^{-jkr}}{4\pi r} \int_I J_v(\rho, 0) \exp \{ -jkr' \cdot \hat{r} \} V\rho^{1/2} d\rho,$$

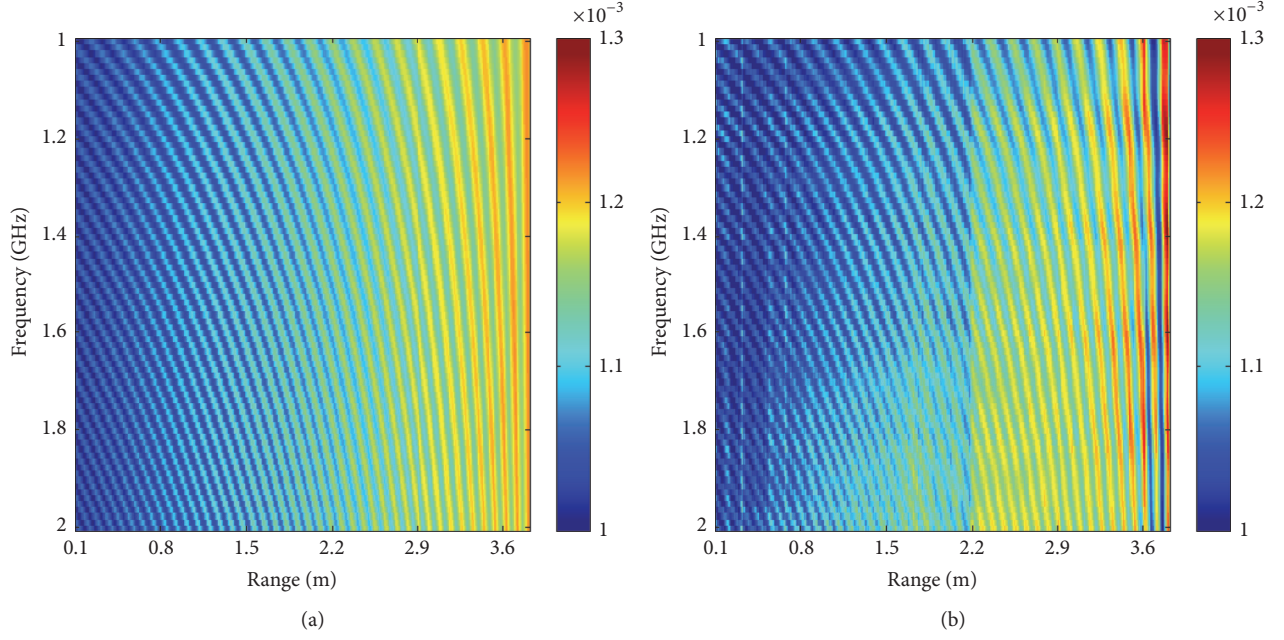


FIGURE 9: Amplitudes of the currents. (a) Simulated currents; (b) real currents.

where  $V = \sqrt{2\pi/jk \sin \theta \sin \alpha}$  and  $\mathbf{r}'$  is the location vectors of currents on  $L1$ .

From (10) we can see that the characteristics of the scattering fields from the flank in lit region are mainly determined by the currents on  $L1$ . Similarly, the characteristics of the scattering fields from the flank in shadow region are mainly determined by the currents on  $L1'$ , and the characteristics of the scattering fields from the bottom are mainly determined by the currents on  $I1$  and  $I1'$ . The total fields are the supposition of the three components, as given below.

$$E_v^s = \sum_{m=1}^3 E_m(a_{1m}, \dots, a_{9m}), \quad (11)$$

where  $E_1$  indicates the electric field induced by the currents in lit region;  $E_2$  indicates the electric field induced by the currents in shadow region;  $E_3$  indicates the electric field induced by the currents on the bottom.

Based on (1) and (10), we can derive the analytic expression of the scattering center model at VV polarization. VV means the incident wave and reflected wave are all in vertical polarization. The analysis of the scattering centers corresponding to the currents on  $L1$  is provided. The analysis processes are similar for the cases of  $L1'$ ,  $I1$ , and  $I1'$ , so the repeated contents are ignored here.

Substituting the expressions of currents on  $L1$ ,  $L1'$ ,  $I1$ , and  $I1'$  into (10), we can derive the total scattering fields, as given by (A.1) in the Appendix. Then through the regular computation of the integral along  $\rho$  in (A.1), we can get 5 exponential terms as shown in (12); the five functions are the

five corresponding parametric models of scattering centers contributed by the currents on  $L1$ .

$$\begin{aligned}
 pSC_1 &= e^{j[(a_{13}+a_{19})l+a_{15}]l} \left( \frac{a_{11}l}{2(a_{12}+a_{18})f-2k\mathbf{r}'\cdot\hat{\mathbf{r}}} \right. \\
 &\quad \left. + \frac{a_{11}}{2j(a_{12}+a_{18}-k\mathbf{r}'\cdot\hat{\mathbf{r}})^2 f^2} \right) e^{j[(a_{12}+a_{18})l-k\mathbf{r}'\cdot\hat{\mathbf{r}}+a_{14}]f} \\
 pSC_2 &= e^{-j[(a_{13}-a_{19})l+a_{15}]l} \left( \frac{a_{11}l}{2(a_{12}-a_{18})f+2k\mathbf{r}'\cdot\hat{\mathbf{r}}} \right. \\
 &\quad \left. - \frac{a_{11}}{2j(a_{12}-a_{18}+k\mathbf{r}'\cdot\hat{\mathbf{r}})^2 f^2} \right) \\
 &\quad \cdot e^{-j[(a_{12}-a_{18})l+k\mathbf{r}'\cdot\hat{\mathbf{r}}+a_{14}]f} \\
 pSC_3 &= e^{ja_{15}} \frac{a_{11}}{2j(a_{12}+a_{18}-k\mathbf{r}'\cdot\hat{\mathbf{r}})^2 f^2} e^{ja_{14}f} \\
 pSC_4 &= -e^{-ja_{15}} \frac{a_{11}}{2j(a_{12}-a_{18}+k\mathbf{r}'\cdot\hat{\mathbf{r}})^2 f^2} e^{-ja_{14}f} \\
 pSC_5 &= \frac{e^{ja_{19}l}}{j(a_{18}f-k\mathbf{r}'\cdot\hat{\mathbf{r}})} \left( -la_{17}-l^2 a_{16} \right. \\
 &\quad \left. + \frac{a_{17}+2la_{16}}{j(a_{18}f-k\mathbf{r}'\cdot\hat{\mathbf{r}})} - \frac{2a_{16}}{j(a_{18}-k\mathbf{r}'\cdot\hat{\mathbf{r}})f^2} \right) \\
 &\quad \cdot e^{j(a_{18}lf-k\mathbf{r}'\cdot\hat{\mathbf{r}})}.
 \end{aligned} \quad (12)$$

TABLE I: Associations between the current model parameters and scattering centers parameters.

Scattering center	Position	Amplitude
SC <sub>1</sub>	$a_{12}, a_{14}, a_{18}, a_{22}, a_{24}, a_{28}$	$a_{11}, a_{12}, a_{13}, a_{15}, a_{18}, a_{19}, a_{21}, a_{22}, a_{23}, a_{25}, a_{28}, a_{29}$
SC <sub>2</sub>	$a_{18}$	$a_{16}, a_{17}, a_{18}, a_{19}$
SC <sub>3</sub>	$a_{28}$	$a_{26}, a_{27}, a_{28}, a_{29}$
SC <sub>4</sub>	$a_{32}, a_{34}, a_{38}$	$a_{31}, a_{32}, a_{33}, a_{35}, a_{38}, a_{39}$

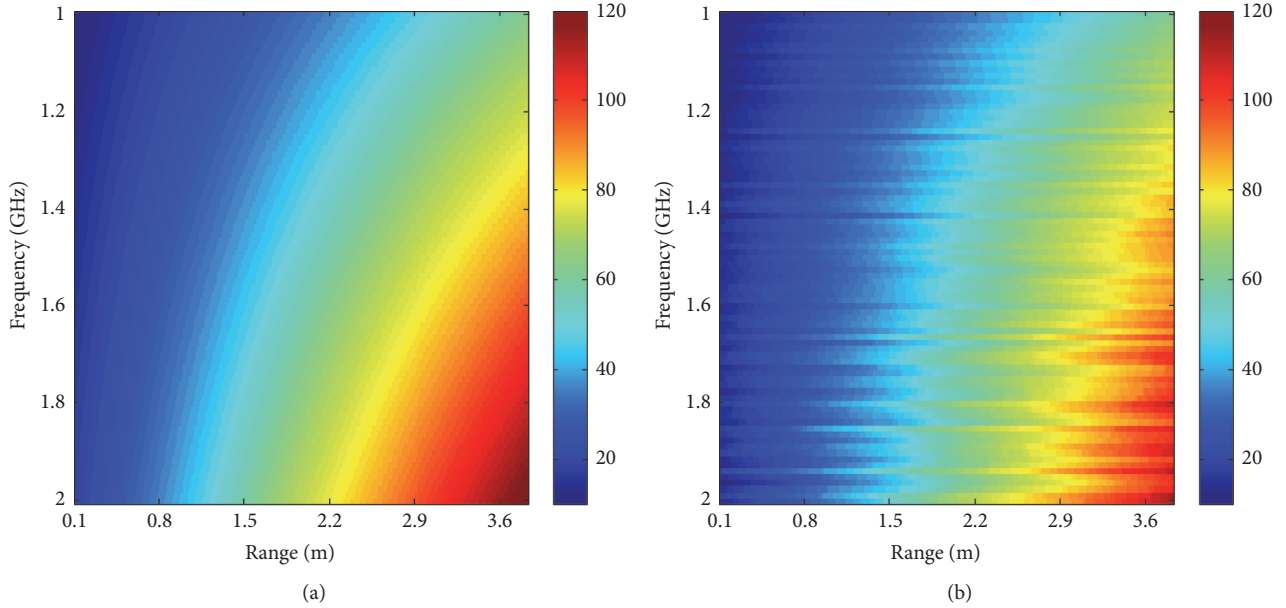


FIGURE 10: Unwrapped phases of the currents. (a) Simulated currents; (b) real currents.

According to the numerical results of the parameters, the components,  $pSC_1$ ,  $pSC_3$ , and  $pSC_4$ , whose amplitudes are quite small compared with the others, can be ignored in the following analysis. The components,  $pSC_2$  and  $pSC_5$ , include the contributions of four scattering centers. The four dominated scattering centers, denoted by SC<sub>1</sub>, SC<sub>2</sub>, SC<sub>3</sub>, and SC<sub>4</sub>, are illustrated in Figure 11. The relationship of the parameters of the model with the amplitudes and locations of scattering centers is listed in Table I.

SC<sub>1</sub> locates at the top of the cone, which is mainly contributed by the components  $pSC_2$  of  $L1$  and  $L1'$ ; SC<sub>2</sub> locates at edges of the bottom in lit region, which is mainly contributed by the components  $pSC_5$  of  $L1$  and  $I1$ ; SC<sub>3</sub> locates at edges of the bottom in shadow region, which is mainly contributed by the components  $pSC_5$  of  $L1'$  and  $I1'$ ; SC<sub>4</sub> locates outside the geometry of the cone, which is mainly contributed by the components  $pSC_2$  of  $I1$  and  $I1'$ , that is, the creeping waves in the shadow region.

#### 4. Validation of the Model

According to the principle of RP, the intensity and position of the peak reflect to a certain extent the scattering amplitude and downrange location of the corresponding scattering center. The accuracy of the derived scattering center model is

validated through comparing the RP simulated by the model (the simulated RP for short) and the data simulated by the scattered fields computed by FE-BI-MLFMA (the real RP for short). Two cone-shaped targets are investigated here. The geometry of target I is the same as the case of Figure 1. The radiuses of bottom disks and spherical tops of target II are the same as target I. The height of target II is  $h = 5.4$  m. Two cases with different parameters setting are investigated.

*Case 1* ( $\theta = 0$ ,  $\phi = 0$ ,  $f = 1\sim 2$  GHz,  $\Delta f = 0.125$  GHz). The simulated RP and the real RP are presented in Figure 12(a). For demonstration of the superiority of this model, the RP obtained by the attributed scattering center model through traditional method are also compared with the simulated RP, as presented in Figure 12(b). The errors of amplitude and locations of the scattering centers are listed in Table 2.

The comparison results demonstrate that the simulated RPs by this model agree well with the real RP. Superior to the exiting model, the scattering center SC<sub>4</sub> induced by creeping waves is precisely characterized by this model.

*Case 2* ( $\theta = 0\sim 10^\circ$ ,  $\Delta\theta = 0.1^\circ$ ,  $\phi = 0$ ,  $f = 1\sim 2$  GHz,  $\Delta f = 0.125$  GHz). The two-dimensional image of the RPs under the continuously changed  $\theta$  (the RP history for short) is investigated. The simulated RP history and the real RP

TABLE 2: Errors of amplitude and locations of the scattering centers.

Case 1	Position errors			Amplitude errors		
Parameters	SC <sub>1</sub>	SC <sub>2</sub>	SC <sub>3</sub>	SC <sub>1</sub>	SC <sub>2</sub>	SC <sub>3</sub>
Current model	0.19λ	0.13λ	0.03λ	0.14 dB	0.02 dB	0.04 dB
Attributed scattering center model	0.19λ	0.13λ	Fail	0.15 dB	0.04 dB	Fail

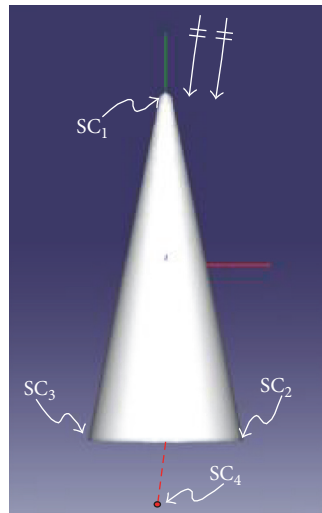


FIGURE 11: Positions of four dominated scattering centers on the target.

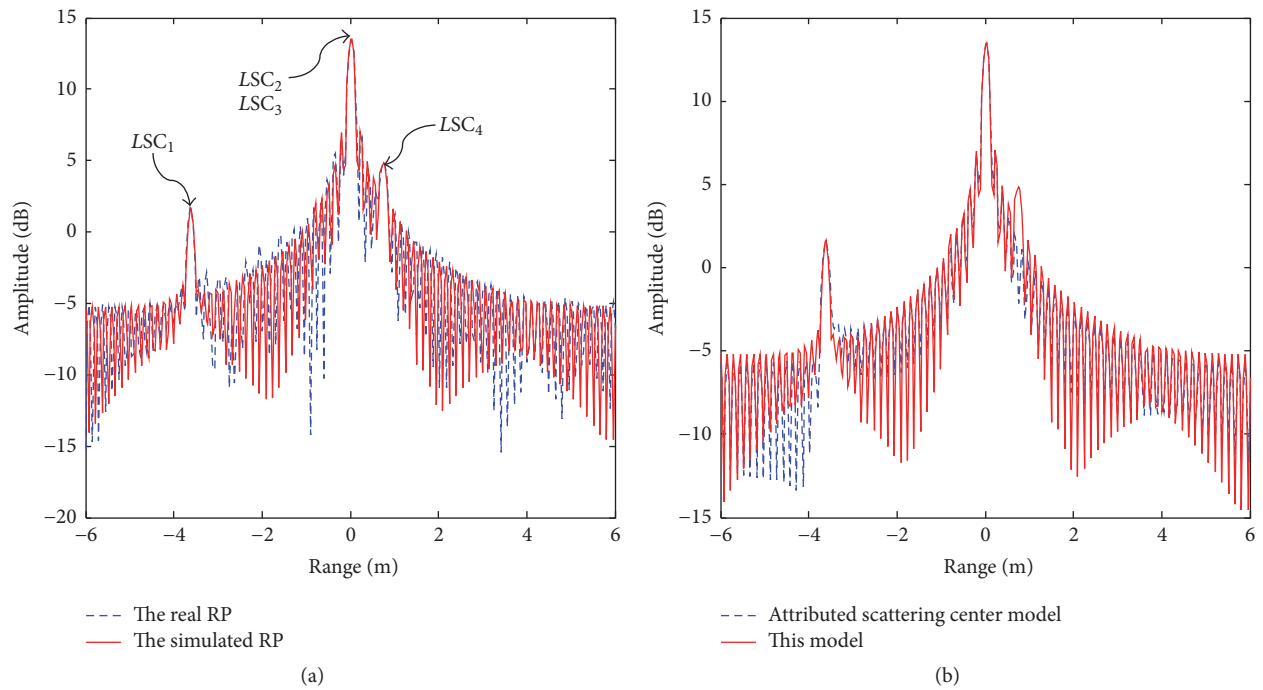


FIGURE 12: Comparison with the RP. (a) Comparison of the simulated RP with the real RP; (b) comparison of the RP obtained by the attributed scattering center model with the simulated RP by this model.

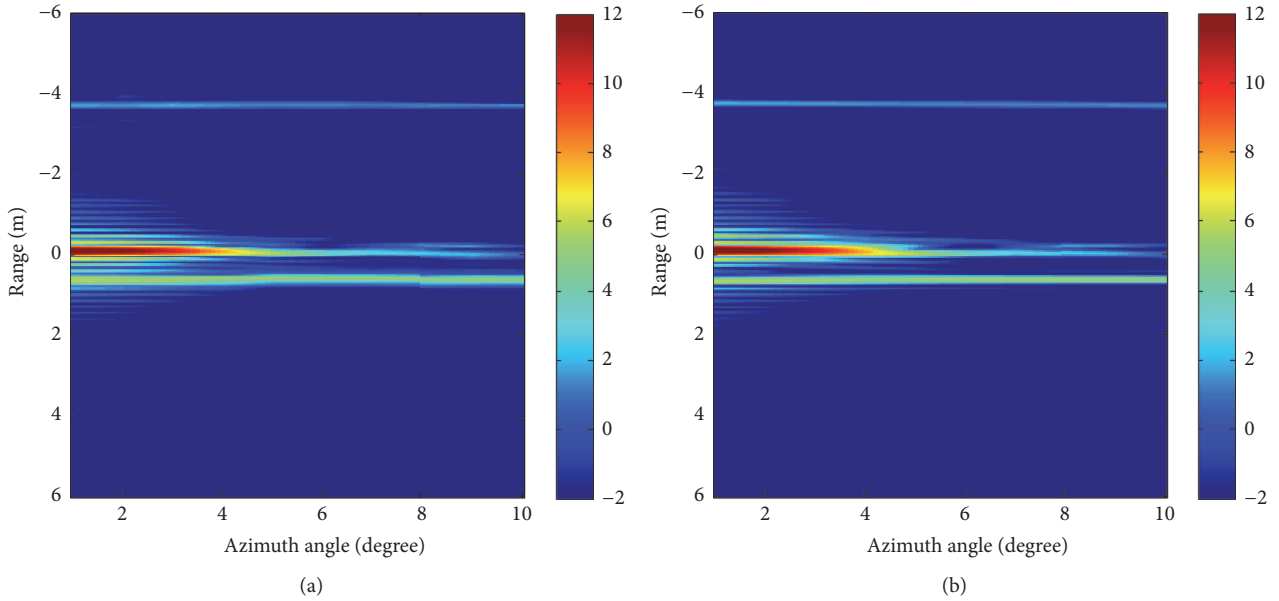


FIGURE 13: RP history of target I. (a) Simulated RP history of target I; (b) real RP history of target I.

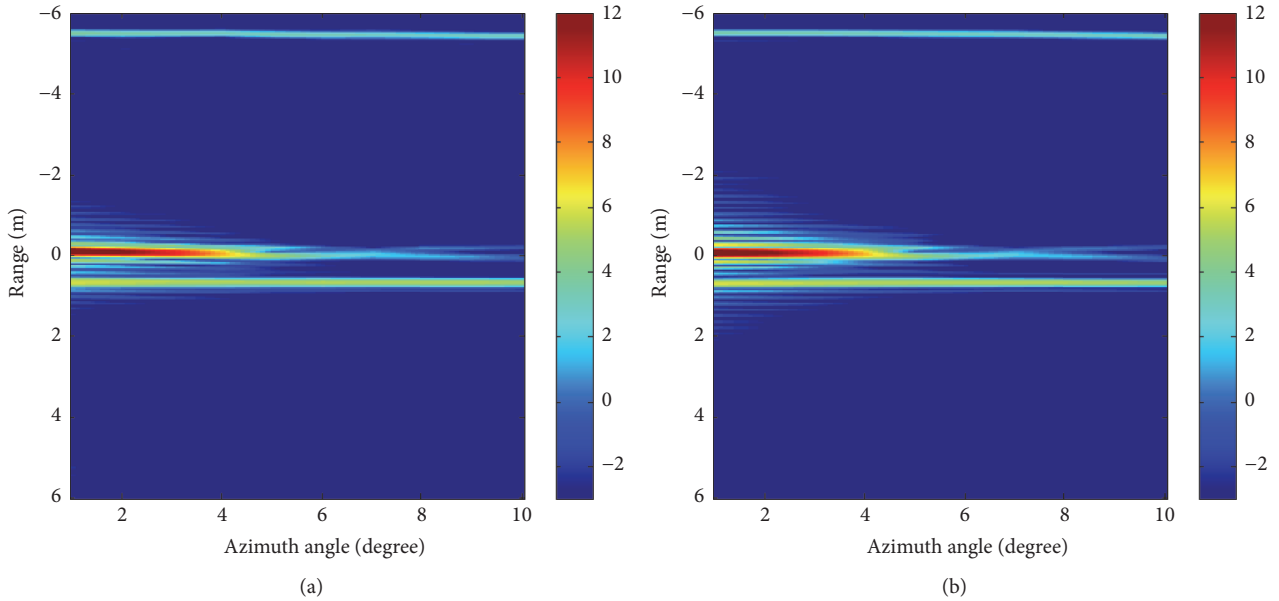


FIGURE 14: RP history of target II. (a) Simulated RP history of target II; (b) real RP history of target II.

history of target I are presented in Figures 13(a) and 13(b). The correlation coefficient of the two images is 86.3%. The RMSE is 2.56 dB.

The simulated RP history and the real RP history of target II are presented in Figures 14(a) and 14(b). The correlation coefficient of the two images is 88.7%. The RMSE is 2.21 dB.

From the images of the RP history of two targets, it can be seen that the simulated results by this model agree well with the results obtained by the full-wave method. The four dominated scattering centers under different aspect angle of LOS

are all precisely characterized. When  $\theta$  is within half conical angle, the  $SC_4$  induced by creeping waves in shadow region is a dominated scattering center; its intensity is even larger than the  $SC_2$  and  $SC_3$  on the edges. Therefore, in these cases,  $SC_4$  should be considered in scattering center modelling.

## 5. Conclusions

The induced currents on cone-shaped targets are investigated in detail in this paper. It is found that scattering characteristics

of the cone-shaped targets are mainly determined by one-dimensional currents on the lines in the plane constructed by the LOS and the rotational axis of the cone. The parametric model of the currents on the lines is built based on their distribution characteristics. Based on the induced currents computed by FE-BI-MLFMA, the parameters of the model are estimated using GA. Then, based on the current model, the scattering center model is derived according to electric field integral expression under far-field condition. This model is suitable for cone-shaped targets with different cone angle and height and can precisely describe scattered waves under arbitrary incident directions.

The precision of this model is validated by the RPs under different aspect angles of LOS. The RPs simulated

by this model agree well with the RP simulated by the scattered fields computed by FE-BI-MLFMA. The location errors of scattering centers are less than half wavelength, the amplitude errors are less than 1dB. The comparison results between this model and the attributed scattering center model show that this model is of higher accuracy, especially in describing the scattering centers contributed by creeping waves.

## Appendix

Substitute (1), (2), and (3) into (10); then the electric field can be expressed as

$$E_1 = -jkZV \frac{e^{-jkr}}{4\pi r} \left( \int_l^0 a_{11}\rho \sin(a_{12}f\rho + a_{13}\rho + a_{14}f + a_{15}) \cdot \exp(j(a_{18}f\rho + a_{19}\rho - k\mathbf{r}' \cdot \hat{\mathbf{r}})) d\rho \right. \\ \left. + \int_l^0 a_{16}\rho^2 \exp(j(a_{18}f\rho + a_{19}\rho - k\mathbf{r}' \cdot \hat{\mathbf{r}})) d\rho + \int_l^0 a_{17}\rho \exp(j(a_{18}f\rho + a_{19}\rho - k\mathbf{r}' \cdot \hat{\mathbf{r}})) d\rho \right) = -jkZV \frac{e^{-jkr}}{4\pi r} (A_1 \\ + A_2 + A_3) \quad (\text{A.1})$$

$$A_1 = \int_l^0 a_{11}\rho \sin(a_{12}f\rho + a_{13}\rho + a_{14}f + a_{15}) \cdot \exp(j(a_{18}f\rho + a_{19}\rho - k\mathbf{r}' \cdot \hat{\mathbf{r}})) d\rho = \frac{a_{11}(l+1)}{2} \\ \cdot \exp\left(j\left(\left(a_{12} + a_{18}\right)fl + a_{14}f + \left(a_{13} + a_{19}\right)l - k\mathbf{r}' \cdot \hat{\mathbf{r}} + a_{15}\right)\right) - \frac{a_{11}(l+1)}{2} \\ \cdot \exp\left(-j\left(\left(a_{12} - a_{18}\right)fl + a_{14}f + \left(a_{13} - a_{19}\right)l + k\mathbf{r}' \cdot \hat{\mathbf{r}} + a_{15}\right)\right) \quad (\text{A.2})$$

$$A_2 = \int_l^0 a_{17}\rho \exp(j(a_{18}f\rho + a_{19}\rho - k\mathbf{r}' \cdot \hat{\mathbf{r}})) d\rho = a_{17}(l+1) \cdot \exp(j(a_{18}fl + a_{19}l - k\mathbf{r}' \cdot \hat{\mathbf{r}})) \quad (\text{A.3})$$

$$A_3 = \int_l^0 a_{16}\rho^2 \exp(j(a_{18}f\rho + a_{19}\rho - k\mathbf{r}' \cdot \hat{\mathbf{r}})) d\rho = a_{17}(l^2 + 2l + 1) \cdot \exp(j(a_{18}fl + a_{19}l - k\mathbf{r}' \cdot \hat{\mathbf{r}})). \quad (\text{A.4})$$

## Competing Interests

The authors declare that there is no competing interests regarding the publication of this paper.

## Acknowledgments

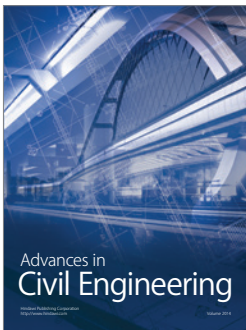
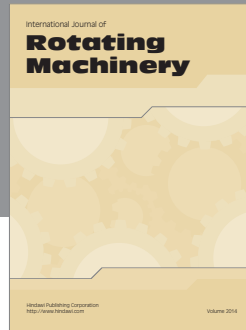
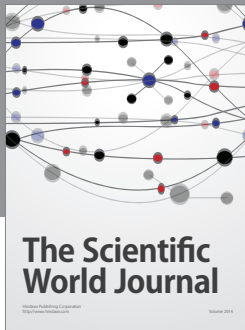
This work was supported by the National Natural Science Foundation of China (Grants nos. 61471041, 61421001, and 61671059).

## References

- [1] J. B. Keller, "Geometrical theory of diffraction," *Journal of the Optical Society of America*, vol. 52, no. 2, pp. 116–130, 1962.
- [2] Q.-Y. Qu, K.-Y. Guo, and X.-Q. Sheng, "Scattering centers induced by creeping waves on streamlined cone-shaped targets in bistatic mode," *IEEE Antennas and Wireless Propagation Letters*, vol. 14, pp. 462–465, 2015.

- [3] M. McClure, R. C. Qiu, and L. Carin, "On the superresolution identification of observables from swept-frequency scattering data," *IEEE Transactions on Antennas and Propagation*, vol. 45, no. 4, pp. 631–641, 1997.
- [4] M. A. Koets and R. L. Moses, "Feature extraction using attributed scattering center models on SAR imagery," in *Algorithms for Synthetic Aperture Radar Imagery VI*, vol. 3721 of *Proceedings of SPIE*, Orlando, Fla, USA, August 1999.
- [5] S. Liu, R. Zhan, J. Zhang, and Z. Zhuang, "Radar automatic target recognition based on sequential vanishing component analysis," *Progress in Electromagnetics Research*, vol. 145, pp. 241–250, 2014.
- [6] Y. He, S. Y. He, Y. H. Zhang, G. J. Wen, D. F. Yu, and G. Q. Zhu, "A forward approach to establish parametric scattering center models for known complex radar targets applied to SAR ATR," *IEEE Transactions on Antennas and Propagation*, vol. 62, no. 12, pp. 6192–6205, 2014.
- [7] H.-C. Chiang, R. L. Moses, and L. C. Potter, "Model-based classification of radar images," *IEEE Transactions on Information Theory*, vol. 46, no. 5, pp. 1842–1854, 2000.

- [8] X. Zhang, J. Qin, and G. Li, "SAR target classification using bayesian compressive sensing with scattering centers features," *Progress in Electromagnetics Research*, vol. 136, pp. 385–407, 2013.
- [9] M. P. Hurst, "Scattering center analysis via prony's method," *IEEE Transactions on Antennas and Propagation*, vol. 35, no. 8, pp. 986–988, 1987.
- [10] J. J. Sacchini, W. M. Steedly, and R. L. Moses, "Two-dimensional prony modeling and parameter estimation," *IEEE Transactions on Signal Processing*, vol. 41, no. 11, pp. 3127–3137, 1993.
- [11] L. C. Potter, D.-M. Chiang, R. Carriere, and M. J. Gerry, "A GTD-based parametric model for radar scattering," *IEEE Transactions on Antennas and Propagation*, vol. 43, no. 10, pp. 1058–1067, 1995.
- [12] X. Yan, J.-M. Hu, G. Zhao, J. Zhang, and J. Wan, "A new parameter estimation method for GTD model based on modified compressed sensing," *Progress in Electromagnetics Research*, vol. 141, pp. 553–575, 2013.
- [13] R. Carrière and R. L. Moses, "High resolution radar target modeling using a modified prony estimator," *IEEE Transactions on Antennas and Propagation*, vol. 40, no. 1, pp. 13–18, 1992.
- [14] L. C. Potter and R. L. Moses, "Attributed scattering centers for SAR ATR," *IEEE Transactions on Image Processing*, vol. 6, no. 1, pp. 79–91, 1997.
- [15] M. J. Gerry, L. C. Potter, I. J. Gupta, and A. D. Van Merwe, "A parametric model for synthetic aperture radar measurements," *IEEE Transactions on Antennas and Propagation*, vol. 47, no. 7, pp. 1179–1188, 1999.
- [16] K.-Y. Guo, Q.-F. Li, X.-Q. Sheng, and M. Gashinova, "Sliding scattering center model for extended streamlined targets," *Progress in Electromagnetics Research*, vol. 139, pp. 499–516, 2013.
- [17] X.-Q. Sheng, J.-M. Jin, J. Song, C.-C. Lu, and W. C. Chew, "On the formulation of hybrid finite-element and boundary-integral methods for 3-D scattering," *IEEE Transactions on Antennas and Propagation*, vol. 46, no. 3, pp. 303–311, 1998.
- [18] X. Q. Sheng, J.-M. Jin, J. Song, W. C. Chew, and C.-C. Lu, "Solution of combined-field integral equation using multilevel fast multipole algorithm for scattering by homogeneous bodies," *IEEE Transactions on Antennas and Propagation*, vol. 46, no. 11, pp. 1718–1726, 1998.
- [19] X.-Q. S. Edward, K.-N. Yung, C. H. Chan et al., "Scattering from a large body with cracks and cavities by the fast and accurate finite-element boundary-integral method," *IEEE Transactions on Antennas and Propagation*, vol. 48, no. 8, pp. 1153–1160, 2000.
- [20] R. F. Harrington, *Field Computation by Moment*, John Wiley & Sons, New York, NY, USA, 1993.
- [21] W. B. Gordon, "High frequency approximations to the physical optics scattering integral," *IEEE Transactions on Antennas and Propagation*, vol. 42, no. 3, pp. 427–432, 1994.
- [22] Y. M. Wu, L. J. Jiang, and W. C. Chew, "An efficient method for computing highly oscillatory physical optics integral," *Progress in Electromagnetics Research*, vol. 127, pp. 211–257, 2012.
- [23] C. Corbel, C. Bourlier, N. Pinel, and J. Chauveau, "Rough surface RCS measurements and simulations using the physical optics approximation," *IEEE Transactions on Antennas and Propagation*, vol. 61, no. 10, pp. 5155–5165, 2013.
- [24] U. d'Elia, G. Pelosi, C. Pichot, S. Selleri, and M. Zoppi, "A physical optics approach to the analysis of large frequency selective radomes," *Progress in Electromagnetics Research*, vol. 138, pp. 537–553, 2013.
- [25] Q. Li, E. J. Rothwell, K.-M. Chen, and D. P. Nyquist, "Scattering center analysis of radar targets using fitting scheme and genetic algorithm," *IEEE Transactions on Antennas and Propagation*, vol. 44, no. 2, pp. 198–207, 1996.
- [26] E. J. Hughes and M. Leyland, "Using multiple genetic algorithms to generate radar point-scatterer models," *IEEE Transactions on Evolutionary Computation*, vol. 4, no. 2, pp. 147–163, 2000.
- [27] T. S. Sijher and A. A. Kishk, "Antenna modeling by infinitesimal dipoles using genetic algorithms," *Progress in Electromagnetics Research*, vol. 52, pp. 225–254, 2005.
- [28] Z.-Q. Meng, "Autonomous genetic algorithm for functional optimization," *Progress in Electromagnetics Research*, vol. 72, pp. 253–268, 2007.
- [29] X.-Q. Sheng and W. Song, *Essentials of Computational Electromagnetics*, John Wiley & Sons, New York, NY, USA, 2012.
- [30] G. Franceschetti and R. Lanari, *Synthetic Aperture Radar Processing*, CRC Press, Boca Raton, Fla, USA, 1999.



**Hindawi**

Submit your manuscripts at  
<https://www.hindawi.com>

